Article:
Stevenson, S.R., Tzokov, S.B., Lahiri, I. et al. (2025) Cryo-EM reconstruction of yeast ADP-actin filament at 2.5 Å resolution. A comparison with vertebrate F-actin. Structure, 33 (3). 435-442.e3. ISSN: 0969-2126

https://doi.org/10.1016/j.str.2024.12.008

Short article

Structure

Cryo-EM reconstruction of yeast ADP-actin filament at 2.5 Å resolution. A comparison with vertebrate F-actin

Graphical abstract

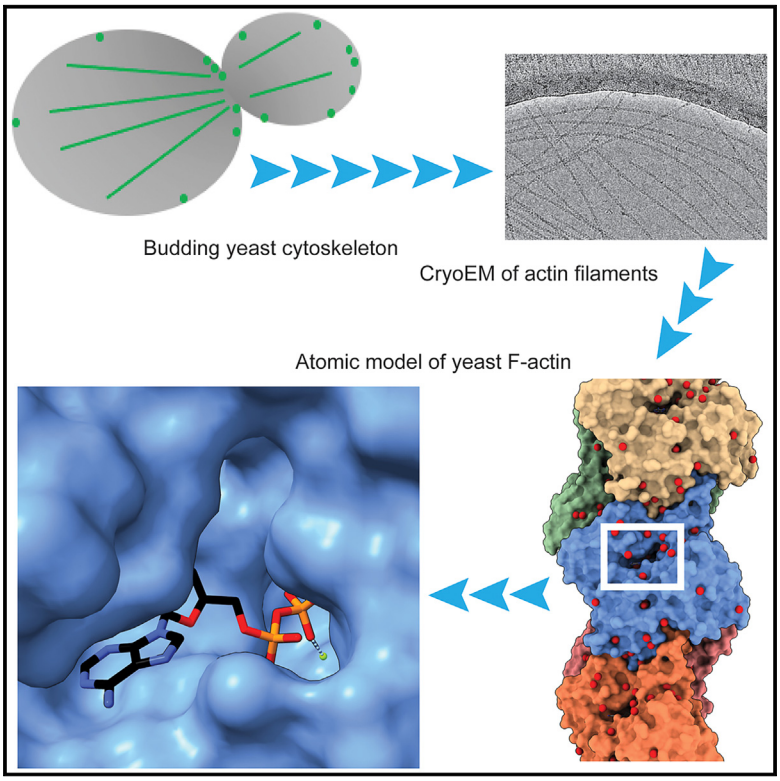

Highlights

- Cryo-EM structure of yeast F-actin at near atomic resolution is determined
- Biophysical differences between yeast and vertebrate actin are explained
- Yeast actin shows a much more open nucleotide binding pocket
- Significant differences between protomer-protomer interactions are observed

Authors

Sarah R. Stevenson, Svetomir B. Tzokov, Indrajit Lahiri, Kathryn R. Ayscough, Per A. Bullough

Correspondence

k.ayscough@sheffield.ac.uk (K.R.A.), p.bullough@sheffield.ac.uk (P.A.B.)

In brief

Stevenson et al. present an atomic model of yeast actin in its filamentous form. The structure helps to explain the biophysical differences between yeast and skeletal actin including stiffness, polymerization interactions and access to the ATP hydrolysis cleft. The structure provides a detailed platform on which to base future genetic studies.

Stevenson et al., 2025, Structure *33*, 435–442
March 6, 2025
https://doi.org/10.1016/j.str.2024.12.008

CellPress

Structure

CellPress
OPEN ACCESS

Short article

Cryo-EM reconstruction of yeast ADP-actin filament at 2.5 Å resolution. A comparison with vertebrate F-actin

Sarah R. Stevenson,[1] Svetomir B. Tzokov,[2] Indrajit Lahiri,[2,3] Kathryn R. Ayscough,[1,*] and Per A. Bullough[2,4,*]
[1]Molecular and Cell Biology, School of Biosciences, University of Sheffield, Sheffield S10 2TN, UK
[2]Molecular Microbiology, School of Biosciences, University of Sheffield, Sheffield S10 2TN, UK
[3]Nucleic Acids Institute, School of Biosciences, University of Sheffield, Sheffield S10 2TN, UK
[4]Lead contact
*Correspondence: k.ayscough@sheffield.ac.uk (K.R.A.), p.bullough@sheffield.ac.uk (P.A.B.)
https://doi.org/10.1016/j.str.2024.12.008

SUMMARY

The core component of the actin cytoskeleton is the globular protein G-actin, which reversibly polymerizes into filaments (F-actin). Budding yeast possesses a single actin that shares 87%–89% sequence identity with vertebrate actin isoforms. Previous structural studies indicate very close overlap of main-chain backbones. Intriguingly, however, substitution of yeast *ACT1* with vertebrate β-cytoplasmic actin severely disrupts cell function and the substitution with a skeletal muscle isoform is lethal. Here we report a 2.5 Å structure of budding yeast F-actin. Previously unresolved side-chain information allows us to highlight four main differences in the comparison of yeast and vertebrate ADP F-actins: a more open nucleotide binding pocket; a more solvent exposed C-terminus; a rearrangement of inter-subunit binding interactions in the vicinity of the D loop and changes in the hydrogen bonding network in the vicinity of histidine 73 (yeast actin) and methyl-histidine 73 (vertebrate actin).

INTRODUCTION

The actin cytoskeleton is a ubiquitous feature of eukaryotic cells, performing diverse functions. The main component of this cytoskeleton is the globular protein actin (G-actin), which reversibly polymerizes into filaments (F-actin). The monomeric and filamentous forms exist in a dynamic and highly regulated equilibrium.

G-actin is a highly conserved protein of ~375 amino acids. Its fold has been categorized into subdomains SD1−SD4 (Figures 1A and 1B), with the N- and C-termini both located in SD1. Critical for function is its ATPase activity, with each monomer bound to one nucleotide in a deep ATP-binding cleft.[2] Binding of ATP, or its hydrolyzed form ADP, is stabilized by a divalent cation in the cleft near the terminal phosphate of the nucleotide. The hydrolysis of ATP occurs rapidly upon polymerization, but release of the γ-phosphate (P_i) is not immediate, resulting in ADP-P_i in the cleft along a segment of the filament. ATP hydrolysis is irreversible, and nucleotide exchange only occurs in the G-actin form.[3]

Within a filament, the helically arranged actin monomers are oriented in the same direction, conferring an overall polarity (Figure 1C). The two ends of a filament have different rates of polymerization, with a fast-growing "barbed" end and a slow growing "pointed" end (also referred to as plus and minus ends, respectively). Because one end of the filament elongates more rapidly than the other, this results in a gradient of bound nucleotide along the length of the filament, with ADP in the cleft of the oldest regions of the filament; ADP-P_i in newer sections; and a small number of ATP-bound monomers at the actively growing filament end.[4,5]

On incorporation into a filament, an actin monomer undergoes a conformational change that can be thought of as "flattening." This is achieved by the relative rotation of the two major domains of the protein found on either side of the cleft (SD1+SD2 and SD3+SD4) by approximately 20° (Figures 1A and 1B).[6] This activates ATP hydrolysis by a subtle reorganization of the active site, increasing its catalytic activity by several-thousand fold.[7] A key factor in this increased catalytic activity is the repositioning of Gln137 and His161 relative to the γ-phosphate of ATP.[6] These residues each anchor a water molecule that plays an active role in the nucleophilic attack on the γ-phosphate during ATP hydrolysis.[1,8]

A shallow barbed end groove between SD1 and SD3 is the binding site for several actin binding proteins.[9,10] The groove includes a region referred to as the W loop (residues 165–172). Other distinct structural features of the protein backbone are the H loop (residues 262–272, located between SD3 and SD4) and the DNase I binding loop (D loop; residues 40–50 in SD2, [Figures 1A and 1B]). The D loop, H loop and N-terminus are highly mobile in both G- and F-actin forms.[11] As well as flattening of the molecule, another notable change upon polymerization is

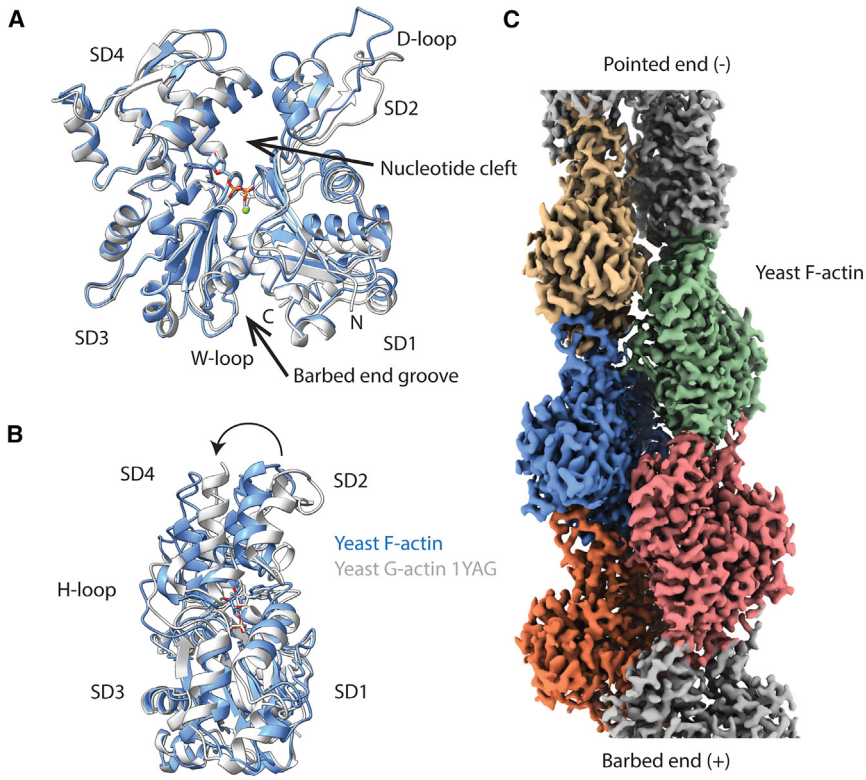

Figure 1. Cryo-EM structure of yeast F-actin at 2.5 Å resolution

(A) Backbone of a single F-actin protomer (blue) compared with G-actin (from yeast G actin-gelsolin complex).[1] A global best fit was performed. Subdomains 1–4 are labeled SD1−SD4. The ADP is shown in stick form along with the Mg^{2+} (green).

(B) View of the protomer rotated approximately 90° from (A). In this view a best fit was performed on SD1 and SD3 only. SD2 and SD4 can be seen to undergo a ∼20° rotation in the G to F transition (curved arrow), leading to overall "flattening" of the structure.

(C) Cryo-EM reconstruction of a segment of the F-actin filament. Five protomers are shown in color with the continuing subunits of the filament in dark gray. The model based on the 5 colored protomers has been deposited with PDB ID: 9GO5. The central protomer (blue) is used in subsequent figures. (See Figures S1–S3, Videos S1 and S2).

the reconfiguration of the D loop,[6] which is a major player in inter-filament contacts (Figure 1A).

The budding yeast *S. cerevisiae* possesses only a single actin isoform, which shares 87%–89% sequence identity (94%–96% sequence similarity) with vertebrate actin isoforms. X-ray crystallographic studies have also found the G-actin structures of yeast and vertebrates to be highly similar.[1] However, substitution of the yeast gene for the vertebrate β-cytoplasmic isoform severely disrupts cell function,[12] and substitution with the vertebrate skeletal muscle isoform is lethal.[13] Direct comparison of dynamics *in vitro* have indicated that yeast actin nucleates more efficiently than skeletal muscle actin in certain ionic environments, and that yeast F-actin exhibits increased fragmentation compared to skeletal muscle F-actin.[14–16] It has also been noted that yeast F-actin does not exhibit the Mg^{2+}-dependent stiffness/rigidity of skeletal muscle actin.[17] This has been attributed to a single residue substitution (Glu167Ala) possibly weakening the filament's interaction with a stiffness-associated cation.[18] Differences have also been observed between yeast and muscle F-actins in their interactions with some binding partners. For instance, yeast F-actin binds phalloidin more rapidly but more weakly than skeletal muscle actin[19] and has a lower affinity for muscle myosin, which it also activates more weakly.[20,21]

The C-terminal region (SD1) and D loop (SD2) have also been implicated in functional differences between isoforms. Both these regions exhibit considerable flexibility and are important for intra-strand protomer-protomer interactions. Fluorescent and phosphorescent labeling of Cys374 have indicated that the C-terminus of yeast F-actin is more flexible and more exposed to the surrounding environment than the C-terminus of skeletal muscle F-actin.[22] The D loop is susceptible to proteolytic cleavage by the protease subtilisin between Met47 and Gly48 of the D loop.[23] The rate of subtilisin digestion of yeast F-actin is approximately 10-fold faster than muscle actin, suggested to indicate greater flexibility compared with the D loop of the skeletal muscle isoform.[15] This has implications for the stability of the intra-strand interactions of yeast F-actin since the D loop is the major contact site between neighboring protomers within the same strand.

While there are now multiple published structures for skeletal muscle F-actin with resolution of 5 Å or better[5,7,8,11,24,25] the resolution of yeast F-actin structure has not been reported past ∼20 Å[26–28] until very recently.[17] The key noted differences between earlier density maps and a rabbit skeletal muscle F-actin map of comparable resolution were that yeast F-actin appeared to have reduced inter-strand connectivity as well as a more open nucleotide binding cleft.[26] These observed differences have since been cited as explanations for the biochemical traits of yeast F-actin.[22,29] However, these observations were based on maps in which the only features that could be resolved were individual protomers and the position of the ATP-binding cleft, and therefore require re-investigation with the more advanced technology now available. A more recent paper based on comparisons of ∼4.5 Å resolution structures of wild-type yeast actin and rabbit actin describes apparent differences in the conformation of the D loop, but these proposed differences also require much higher resolution data to be testable.[17]

Our cryoelectron microscopy (cryo-EM) yeast F-actin structure is considerably improved in resolution, with detailed information including side chain conformers and water molecules. Using our 2.5 Å map and an atomic model constructed from it, we investigated whether the formerly reported differences between vertebrate skeletal muscle F-actin and yeast F-actin were consistent with these higher resolution structural data. We find a more open nucleotide binding pocket; a more solvent exposed C-terminus; a rearrangement of inter-subunit binding

interactions via the D loop and changes in the hydrogen bonding network near His73.

RESULTS AND DISCUSSION

Saccharomyces cerevisiae actin (referred to henceforth as yeast actin) was expressed from its single actin-encoding gene *ACT1* in a *Pichia pastoris* expression system according to the method of Hatano and colleagues.[30] In this system actin is expressed and purified as a fusion with the actin monomer binding protein thymosin-β4. When this fusion protein is expressed, the thymosin-β4 sequesters the recombinant G-actin, preventing interactions with both the barbed and pointed end of the monomer and also preventing co-polymerization with *Pichia* actin. Following purification, the actin was cleaved from thymosin-β4 at its normal C-terminal residue using chymotrypsin. Yeast actin was then polymerized for cryo-EM analysis (Figure S1A).

We reconstructed the yeast actin filaments with Mg^{2+} and ADP (Figure 1C; Video S1). We selected 2,047,208 particles from 2,540 micrographs and after rounds of 2D classification 1,368,572 particles were retained for further processing. These particles were subjected to rounds of 3D helical refinement within CryoSPARC[31] giving a map with a global resolution of 2.5 Å (Figures S1B–S1F; Table S1).

The reconstruction showed the ADP and Mg^{2+} well resolved, along with most amino acid side chains and a number of waters (Figures 2A, 2B, and S2B; Video S1). Densities were weakest (with correspondingly high model B-factors [Figure S1B]) in the D loop, peripheral regions of SD4, in the C-terminal region and at the N-terminus, where residues 1 to 5 were not built; nevertheless the full D loop was still well-resolved in comparison to a number of reported vertebrate F-actin structures (Figures S1E and S3C–S3F).

Comparison of yeast G- and F-actin conformations

A number of X-ray structures of G-actin in complex with other proteins or modified to prevent polymerization have been described; structures of F-actin can be compared with G-actin in various nucleotide-bound states for *Plasmodium*, avian and mammalian proteins (e.g., PDB ID: 6I4W, 4CBU, 7W4Z, 7W51, IJ6Z, and 1NWK). Many of these G-actin structures have disordered D loops and/or C-termini. However, for yeast actin we now have a rare opportunity to compare high resolution and well-ordered structures of both ATP-bound G- and ADP-bound F-actin within a single species (Figures 1A, 1B, S2, and S3).

A global comparison of the overall fold of one yeast F-actin subunit and that of yeast ATP-G-actin (in complex with gelsolin segment-1[1]) is shown in Figures 1A and S4CE; Video S2. A similar comparison is shown for rabbit ATP G-actin with chicken ADP F-actin (structures were chosen as they have relatively ordered D loops) in Figures S4D and S4F. It should be noted that the sequences of rabbit and chick actin are identical, so that we can use either when comparing vertebrate skeletal actins with yeast actin. The G-actin structures are very similar (Figures S4A and S4B), with the main significant difference in the region of the D loop; this could reflect the effect of DNaseI binding to the D loop in the rabbit G-actin crystal structure. As previously described,[6] on incorporation into a filament, the G-actin monomer flattens. This is illustrated in Figure 1B and Video S2 where a best fit of SD1 and SD3 reveals an approximately 20° movement of the other subdomains (Figure 1B). The G-F transition in yeast is slightly more pronounced in SD4 than it is in the vertebrate equivalent, whereas it is slightly less so in SD1 (Figures S4C–S4F).

In both the yeast and vertebrate G-F transition, changes in the polypeptide backbone around the nucleotide binding cleft are relatively small (Figures 1A and S4C–S4E; Video S2). The conformational change is proposed to activate ATP hydrolysis by a subtle reorganization of the active site that increases its catalytic activity by several-thousand fold.[7] A key factor in this increased catalytic activity is the repositioning of Gln137 and His161 relative to the γ-phosphate of ATP.[1,6,8] In yeast actin, around the nucleotide binding site we see rearrangements of Gln137 and His161 similar to those reported for avian F-actin with an ATP mimic. However, in our ADP-Mg^{2+} F-actin structure we also see a rotation of the side chain of D154 relative to that in ATP G-actin (Figure S2A).[7] This is similar to that seen in a chicken ADP F-actin structure.[24] Thus, within the limitations of a 2.5 Å resolution map, we see no major differences in the post-catalytic structures of yeast and vertebrate F-actin around the nucleotide.

Comparison with mammalian, avian, and previous yeast F-actin models

Overall architecture

The overall subunit fold is near-identical to that of other recently determined structures from rabbit and chicken with backbone root-mean-square deviation (RMSD) of ∼0.3–∼0.6 Å; this is unsurprising given the close sequence identity between actin isoforms (Figures S4A and S4B). It is notable, however, that the RMSD between our yeast structure and the yeast structure of Xu et al.[17] is at the higher end of the range at ∼0.6 Å. This significant deviation reflects the uncertainties associated with a 4.5 Å versus a 2.5 Å resolution structure. Locally, between the two structures, deviations are significantly greater, by up to 2–3 Å in some cases (Figures S5B–S5H). Notably, in the D loop the 4.5 Å structure has very high B-factors (up to 210 $Å^2$) whereas our 2.5 Å structure has much lower B-factors (up to 60 $Å^2$), thus revealing the backbone and sidechains in their more likely position (Figure S5D). When analyzing the function of key parts of the structure, such as the D loop, our structure provides a more accurate platform from which to work.

Within the filament, the axial rise and helical twist between subunits is also similar to vertebrate F-actin at 27.6 Å and −167.2°. We see no significant difference in inter-strand connectivity between yeast and other F-actins. The largest differences in backbone conformation are found in the C-terminal region and the D loop; it is particularly notable that the C-terminal region in the rabbit ADP-Mg^{2+} F-actin determined by Oosterheert et al.[5] adopts a significantly different arrangement compared with both yeast actin and other comparable vertebrate actin structures (Figure S4J).

Nucleotide binding site

The nucleotide binding site contains density corresponding to ADP (Figure 2A) and lacks any density corresponding to a γ-phosphate, indicating this structure represents the ADP state of F-actin. Density for a putative Mg^{2+} ion is also indicated, along with slightly noisier density consistent with the approximate

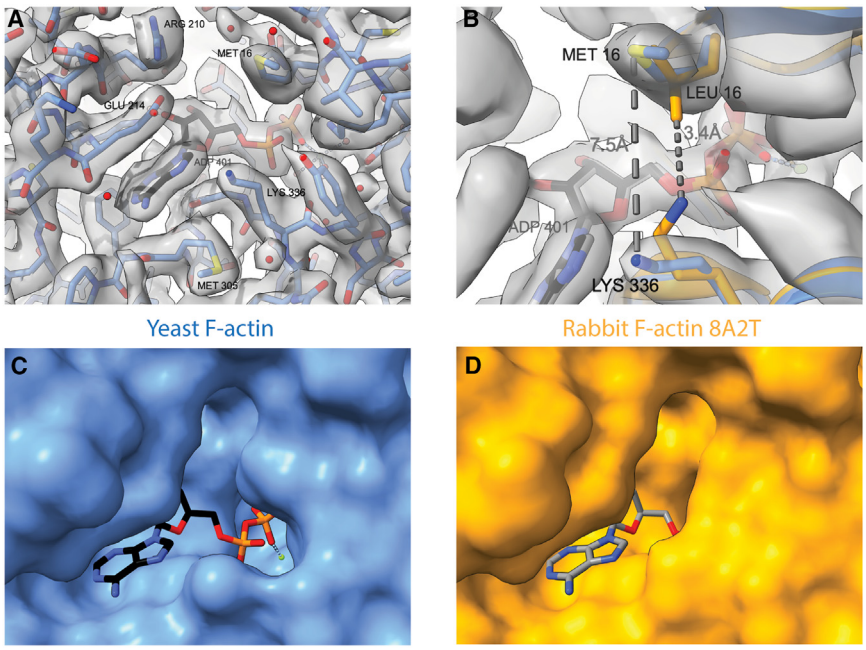

Figure 2. Comparison of the nucleotide binding pocket in yeast and mammalian F-actin

(A) Cryo-EM density in the vicinity of the binding pocket of yeast F-actin with the fitted atomic model (actin carbon—cornflower blue; ADP carbon—black; oxygen or water—red; nitrogen—dark blue; sulfur—yellow; phosphorous—orange).

(B) Comparison of critical amino acids 16 and 336 near the binding site. Yeast and mammalian ADP are black and gray, respectively. In yeast actin, Met16 and Lys336 are separated by a greater distance than the respective residues in mammalian actin, leading to a more open binding pocket.

(C) Surface rendering of the nucleotide binding pocket in yeast, with the ADP shown in stick form.

(D) The equivalent binding pocket in mammalian actin[5] is closed off through the Leu16-Lys336 interaction. (See Figure S2 and Video S1).

positions of coordinating waters (Figure S2B). We have not put constraints on the positions of these waters in the model.

Comparison with high resolution structures of vertebrate F-actin indicates a more open nucleotide binding cleft in yeast actin (Figures 2B–2D); this is consistent with the observations of Orlova et al.[26] on negatively stained fibers. The residues "shielding" the entrance to the skeletal actin site are Leu16 and Lys336 that are in van der Waals contact; in yeast this contact is broken with a Leu16Met substitution and the adoption of a different side chain conformation of Lys336 (Figure 2B). The more open nucleotide binding pocket could affect ATP hydrolysis and phosphate release—this could be tested with a Met16Leu yeast actin mutant. However, it is notable that we see little difference (within the limits of resolution) in the positions of the catalytically important residues such as Gln137 and His161 in the post-catalytic ADP F-actin structures (Figure S2A; Video S1).

His73 is suggested to control P_i release after ATP hydrolysis during polymerization. His73 is a 3-methylhistidine in vertebrate and *Plasmodium* actin[32,33] but is unmethylated in yeast.[34,35] The density in our reconstruction is consistent with this. Figure 3 shows a comparison of residues near His73 for yeast and rabbit actin. In the skeletal muscle F-actin the methylated His73 does not appear to form strong interactions with any neighboring residues whereas in yeast the unmethylated His73 is in a more favorable position to hydrogen bond with the main chain oxygen of Gly158. Glu72 appears to adopt two alternative rotamers, one as also seen in vertebrate actin (Figure 3C) and one as shown in Figure 3B. The slight shift in position of His73, Gly158 and Val159 is accompanied by a shift of the main chain around Arg177-Asp179 by ~0.5 Å. This prevents a steric clash and leads to a sparser hydrogen bonding network. Arg177 maintains an interaction with Asn111 and thus represents the closed "gate" conformation for γ-phosphate release.[36] In our model Oδ2 of Asp179 reaches within 3.8 Å of Nδ1 of His73 (compared with 4.5 Å for 8A2T); given the uncertainty in the map it is possible that Asp179 can adopt a geometry and distance to form a salt bridge with His73, while Asp184 appears unlikely to form any interaction.[37] We see no significant difference in the His73 imidazole ring, or salt bridge with Asp184 despite this being previously predicted.[38]

The W loop, D loop, and H loop

A crucial interaction in the longitudinal direction of the filament is that between the W loop (165–172) and D loop (40–50) of respective subunits; the W loop is a region of sequence divergence, with substitutions at positions 167,169, and 170 (Figure 4). A water forms a central hub in an extended network in rabbit actin (marked HOH565) in Figure 4C) that appears to be absent in yeast actin as a result of substitutions at positions 167 and 292 (Figure 4). Thus, in yeast, the W loop is less constrained by the intra-subunit H-bond network (Figures 4B and 4C) and can therefore shift its backbone toward the D loop in the neighboring subunit, with the D loop also shifting. The rearrangements near the W loop in yeast enable a hydrogen bonding interaction with Gln49 of the D loop in the neighboring subunit (Figure 4). The overall impact of these changes is that the rabbit actin has two regions of extensive H-bonding near Asp292 and Tyr169 while the yeast actin has only one, near Tyr169. This "loosening" of the hydrogen bonding anchor of the W loop could contribute to the apparent overall increased flexibility of yeast actin filaments.[16,18] Xu et al., using a model-based sharpening method,[17,39] have attributed the stiffening of rabbit muscle F-actin to the presence of a coordinated Mg^{2+} ion indirectly bound to Glu167 via a water molecule. However, models of skeletal actin (e.g., PDB ID:8A2T[5]) that have sufficiently high resolution to reveal water molecules, do not indicate such an arrangement.

The difference in longitudinal contact strength was previously suggested to be due to the Glu167Ala substitution in yeast actin.[40] While it is the case that Ala167 in yeast does not participate in a salt bridge it is notable that Ser170 (Ala170 in skeletal muscle actin) facilitates additional H-bond interactions with the

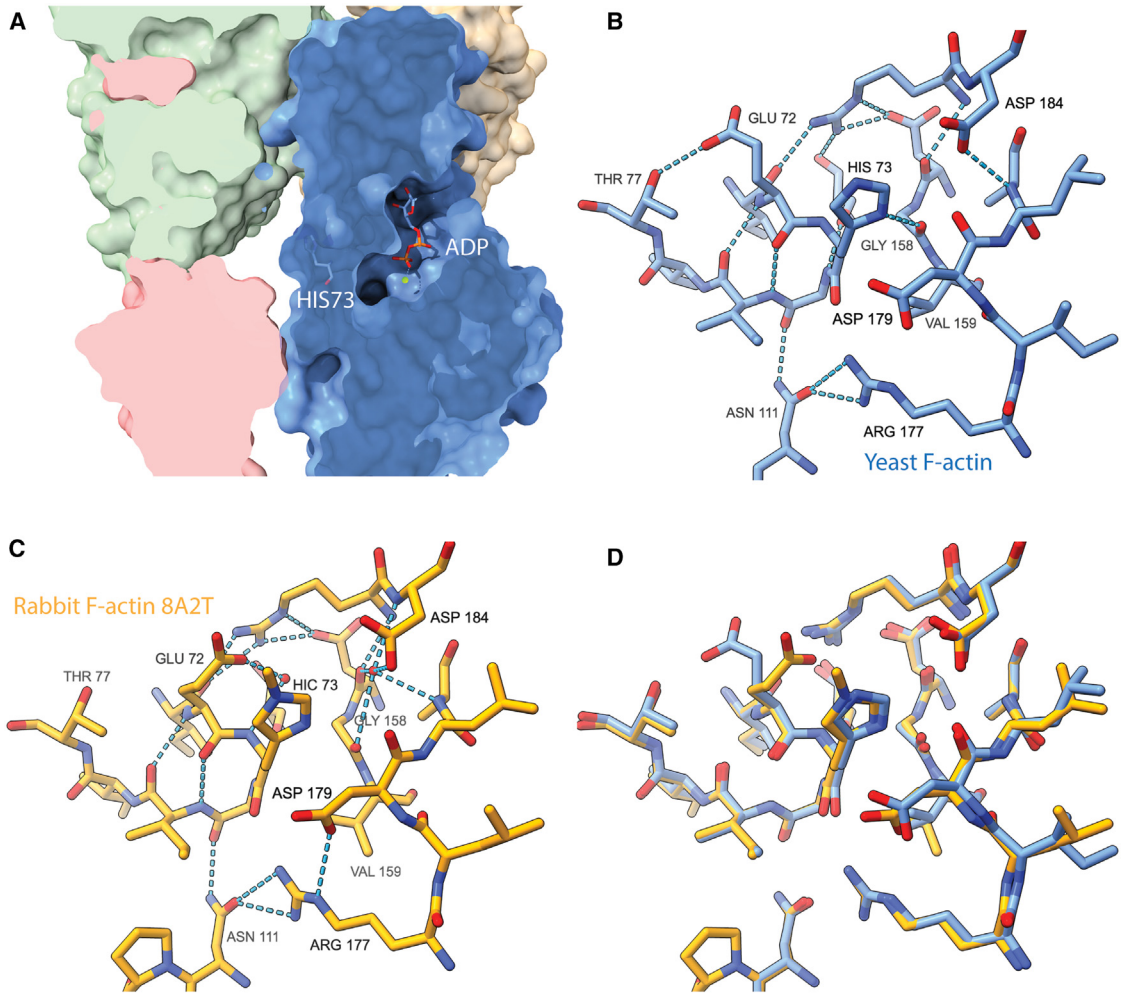

Figure 3. Comparison of yeast and mammalian actin near His73

(A) Cross section of yeast F-actin showing molecular surfaces. The nucleotide binding site is indicated with the position of the ADP and Mg^{2+} and His73. His73 is suggested to control the release of P_i after ATP hydrolysis during polymerization.

(B) Yeast structure near His73, with predicted H-bonds/salt bridges for selected residues. The Glu72 rotamer is shown in one of two possible conformations-the other one is equivalent to that shown in (C). Water molecules hidden.

(C) Equivalent view of the mammalian structure, where His73 is substituted with methyl histidine (HIC 73). Differences in H-bond/salt bridge interactions can be seen when comparing rabbit and yeast F-actin (B).

(D) Alignment of the yeast and mammalian structures. (See Video S1).

D loop (Figures 4A and 4B). If this bonding network is disrupted in a Ser170Cys substitution in yeast, the polymerization rate is reduced.[41] These additional interactions may also account for the apparent increased ordering of the D loop in yeast actin (Figure S1B).

The D loop is susceptible to proteolytic cleavage by subtilisin between Met47 and Gly48 of the D loop (Figures S1B and S1E).[23] The rate of subtilisin digestion of yeast F-actin was reported to be approximately 10-fold faster than muscle actin, and this was suggested to indicate greater flexibility compared with the D loop of the skeletal muscle isoform.[15] The inter-residue bonding in the yeast F-actin structure however does not support the idea of greater flexibility in the D loop region. Rather we would consider that the higher level of proteolysis observed under the reported conditions is possibly due to increased turnover rate of the filaments themselves with subtilisin cleaving the actin monomers following disassembly.

The D loop also interacts with the C-terminus of the adjacent subunit (Figure S6A). A notable feature is the Val43Ile substitution in yeast actin compared to skeletal actin. If Phe375 in the adjacent subunit were to maintain the position adopted in the skeletal actin, this would result in a steric clash; thus, Phe375 adopts the more exposed position seen in yeast. This is consistent with fluorescent and phosphorescent labeling studies of Cys374 indicating that the C-terminus of yeast F-actin is more flexible and more exposed to the surrounding environment.[22] To avoid steric clash between Ile43 and Val139 in the adjacent subunit, the mainchain of the D loop shifts relative to that in chicken actin (Figure S6A). Notable also are Arg39 and His40 that interact with both adjacent inter- and intra-strand protomers

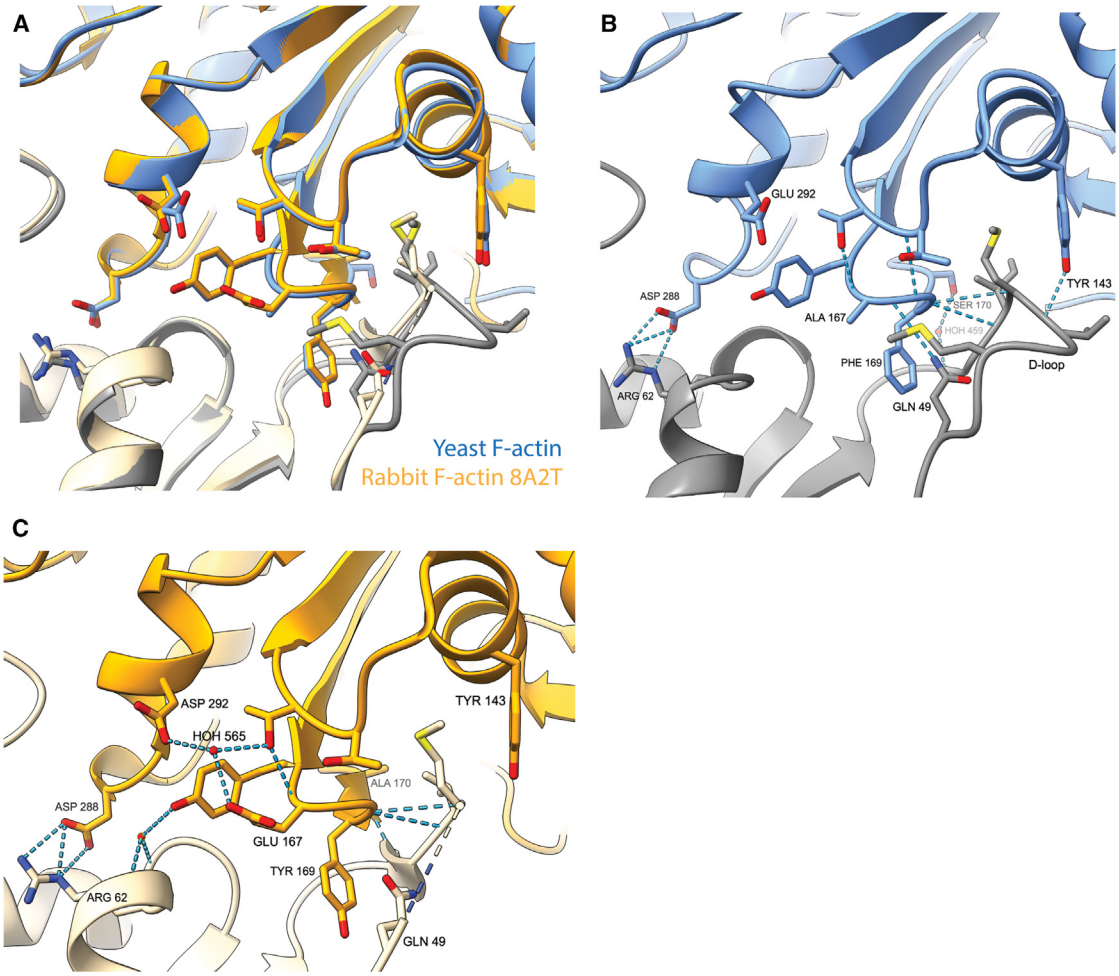

Figure 4. W loop:D loop interactions between subunits-comparison between yeast and mammalian F-actin

(A) Structural alignments of yeast actin (blue/dark gray) and mammalian actin (orange/straw) in the vicinity of the D loop. Some waters hidden.

(B) Key interactions of the D loop of one subunit (dark gray) and a neighboring subunit (including its W loop) (blue) in yeast F-actin. Ser170 interacts with the D loop of the neighboring subunit.

(C) Equivalent interactions in mammalian actin. The D loop is more disordered-un-modeled segment has dashed line. Ala170 is unable to interact with the D loop (see B). A water (HOH 565) may strengthen interactions around residue 292, which is a glutamate in yeast and an aspartate in rabbit. (See Figures S6 and S7).

through a hydrogen bonded network of waters (Figure S6B). Thus, the D loop serves a critical role in bringing together three separate protomers of the filament.

The H loop is also a region of relatively high sequence divergence, with several substitutions between residues 262–274. However, the loop in yeast actin shows only minor shifts in the backbone relative to skeletal actin (Figure S7).

In conclusion, using our 2.5 Å map of yeast actin, we have investigated whether the formerly reported differences between vertebrate skeletal muscle F-actin and yeast F-actin were consistent with our higher resolution structural data. In yeast actin, the more open nucleotide binding pocket and differences in the hydrogen bonding network in the vicinity of histidine 73 may affect ATP hydrolysis and phosphate release; rearrangements of inter-subunit binding interactions in the vicinity of the D loop and W loop are likely to contribute to the increased flexibility of yeast actin filaments. Given the accessible genetics of yeast, our high-resolution structure of F-actin provides a platform for future functional interrogation.

RESOURCE AVAILABILITY

Lead contact

Further information and requests for resources and reagents should be directed to the lead contact, Per A. Bullough (p.bullough@sheffield.ac.uk).

Materials availability

This study did not generate new unique reagents.

Data and code availability

EM maps and molecular structures generated in this study have been deposited at PDB and EMDB databanks under entry codes PDB ID 9GO5, EMD-51491, respectively, and are publicly available as of the date of publication. The accession codes are also listed in the key resources table. The paper does not report original code. Any additional information required to reanalyze the data reported in this paper is available from the lead contact upon request.

ACKNOWLEDGMENTS

We thank Julien Bergeron and Nora Cronin for help with data collection (Francis Crick Institute); Mohan Balasubramanian, Tomo Hatano, and Andrejus Suchenko (University of Warwick) for support in expressing and purifying yeast actin; and Bruce Goode (Brandeis University) and Sarah Harris (University of Sheffield) for valuable discussion. Local data collection and processing was performed in the University of Sheffield, Biosciences EM facility, partly funded through its Imagine: Imaging Life program. K.R.A. was supported by Leverhulme Research Fellowship RF-2021-099\2; S.R.S by a Ph.D. studentship through the BBSRC White Rose DTP Training Program (BB/M011151/1).

AUTHOR CONTRIBUTIONS

Conceptualization, K.R.A and P.A.B.; methodology, K.R.A., P.A.B., S.R.S. S.B.T., and I.L.; experimentation, S.R.S., S.B.T., and I.L.; writing, K.R.A. and P.A.B.; visualization, P.A.B. and K.R.A.; supervision, K.R.A. and P.A.B.; funding acquisition, K.R.A. and P.A.B.

DECLARATION OF INTERESTS

The authors declare no competing interests.

STAR★METHODS

Detailed methods are provided in the online version of this paper and include the following:

- KEY RESOURCES TABLE
- EXPERIMENTAL MODEL AND STUDY PARTICIPANT DETAILS
  - *Pichia pastoris*, used for protein expression
- METHOD DETAILS
  - Yeast actin purification
  - Polymerization of actin for CryoEM
  - CryoEM data collection and image processing
  - Model building and refinement
- QUANTIFICATION AND STATISTICAL ANALYSIS

SUPPLEMENTAL INFORMATION

Supplemental information can be found online at https://doi.org/10.1016/j.str.2024.12.008.

Received: September 17, 2024
Revised: November 19, 2024
Accepted: December 12, 2024
Published: January 10, 2025

REFERENCES

1. Vorobiev, S., Strokopytov, B., Drubin, D.G., Frieden, C., Ono, S., Condeelis, J., Rubenstein, P.A., and Almo, S.C. (2003). The structure of nonvertebrate actin: Implications for the ATP hydrolytic mechanism. Proc. Natl. Acad. Sci. USA *100*, 5760–5765. https://doi.org/10.1073/pnas.0832273100.
2. Kabsch, W., Mannherz, H.G., Suck, D., Pai, E.F., and Holmes, K.C. (1990). Atomic structure of the actin: DNase I complex. Nature *347*, 37–44. https://doi.org/10.1038/347037a0.
3. Carlier, M.-F., and Shekhar, S. (2017). Global treadmilling coordinates actin turnover and controls the size of actin networks. Nat. Rev. Mol. Cell Biol. *18*, 389–401. https://doi.org/10.1038/nrm.2016.172.
4. Bryan, K.E., and Rubenstein, P.A. (2005). An Intermediate form of ADP-F-actin. J. Biol. Chem. *280*, 1696–1703. https://doi.org/10.1074/jbc.m410180200.
5. Oosterheert, W., Klink, B.U., Belyy, A., Pospich, S., and Raunser, S. (2022). Structural basis of actin filament assembly and aging. Nature *611*, 374–379. https://doi.org/10.1038/s41586-022-05241-8.
6. Oda, T., Iwasa, M., Aihara, T., Ma éda, Y., and Narita, A. (2009). The nature of the globular- to fibrous-actin transition. Nature *457*, 441–445. https://doi.org/10.1038/nature07685.
7. Chou, S.Z., and Pollard, T.D. (2019). Mechanism of actin polymerization revealed by cryo-EM structures of actin filaments with three different bound nucleotides. Proc. Natl. Acad. Sci. USA *116*, 4265–4274. https://doi.org/10.1073/pnas.1807028115.
8. Merino, F., Pospich, S., Funk, J., Wagner, T., Küllmer, F., Arndt, H.-D., Bieling, P., and Raunser, S. (2018). Structural transitions of F-actin upon ATP hydrolysis at near-atomic resolution revealed by cryo-EM. Nat. Struct. Mol. Biol. *25*, 528–537. https://doi.org/10.1038/s41594-018-0074-0.
9. Chereau, D., Kerff, F., Graceffa, P., Grabarek, Z., Langsetmo, K., and Dominguez, R. (2005). Actin-bound structures of Wiskott–Aldrich syndrome protein (WASP)-homology domain 2 and the implications for filament assembly. Proc. Natl. Acad. Sci. USA *102*, 16644–16649. https://doi.org/10.1073/pnas.0507021102.
10. Aguda, A.H., Xue, B., Irobi, E., Préat, T., and Robinson, R.C. (2006). The structural basis of actin interaction with multiple WH2/beta-thymosin motif-containing proteins. Structure *14*, 469–476. https://doi.org/10.1016/j.str.2005.12.011.
11. Galkin, V.E., Orlova, A., Vos, M.R., Schröder, G.F., and Egelman, E.H. (2015). Near-Atomic Resolution for One State of F-Actin. Structure *23*, 173–182. https://doi.org/10.1016/j.str.2014.11.006.
12. Karlsson, R., Aspenström, P., and Byström, A.S. (1991). A chicken β-actin gene can complement a disruption of the *Saccharomyces cerevisiae* ACT1 Gene. Mol. Cell Biol. *11*, 213–217. https://doi.org/10.1128/mcb.11.1.213-217.1991.
13. McKane, M., Wen, K.-K., Boldogh, I.R., Ramcharan, S., Pon, L.A., and Rubenstein, P.A. (2005). A mammalian actin substitution in yeast actin (h372r) causes a suppressible mitochondria/vacuole phenotype. J. Biol. Chem. *280*, 36494–36501. https://doi.org/10.1074/jbc.m506970200.
14. Buzan, J.M., and Frieden, C. (1996). Yeast actin: polymerization kinetic studies of wild type and a poorly polymerizing mutant. Proc. Natl. Acad. Sci. USA *93*, 91–95. https://doi.org/10.1073/pnas.93.1.91.
15. Kim, E., Miller, C.J., and Reisler, E. (1996). Polymerization and in vitro motility properties of yeast actin: a comparison with rabbit skeletal α-actin. Biochemistry *35*, 16566–16572. https://doi.org/10.1021/bi9623892.
16. McCullough, B.R., Grintsevich, E.E., Chen, C.K., Kang, H., Hutchison, A.L., Henn, A., Cao, W., Suarez, C., Martiel, J.-L., Blanchoin, L., et al. (2011). Cofilin-linked changes in actin filament flexibility promote severing. Biophys. J. *101*, 151–159. https://doi.org/10.1016/j.bpj.2011.05.049.
17. Xu, X.-P., Cao, W., Swift, M.F., Pandit, N.G., Huehn, A.E., Sindelar, C.V., De La Cruz, E.M., Hanein, D., and Volkmann, N. (2024). High-resolution yeast actin structures indicate the molecular mechanism of actin filament stiffening by cations. Commun. Chem. *7*, 164. https://doi.org/10.1038/s42004-024-01243-x.
18. Kang, H., Bradley, M.J., McCullough, B.R., Pierre, A., Grintsevich, E.E., Reisler, E., and De La Cruz, E.M. (2012). Identification of cation-binding sites on actin that drive polymerization and modulate bending stiffness. Proc. Natl. Acad. Sci. USA *109*, 16923–16927. https://doi.org/10.1073/pnas.1211078109.
19. De La Cruz, E.M., and Pollard, T.D. (1996). Kinetics and thermodynamics of phalloidin binding to actin filaments from three divergent species. Biochemistry *35*, 14054–14061. https://doi.org/10.1021/bi961047t.
20. Greer, C., and Schekman, R. (1982). Calcium control of *Saccharomyces* cerevisiae actin assembly. Mol. Cell Biol. *2*, 1279–1286. https://doi.org/10.1128/mcb.2.10.1279-1286.1982.
21. Cook, R.K., Root, D., Miller, C., Reisler, E., and Rubenstein, P.A. (1993). Enhanced stimulation of myosin subfragment 1 ATPase activity by addition of negatively charged residues to the yeast actin NH2 terminus. J. Biol. Chem. *268*, 2410–2415.
22. Prochniewicz, E., and Thomas, D.D. (1999). Differences in structural dynamics of muscle and yeast actin accompany differences in functional

interactions with myosin. Biochemistry *38*, 14860–14867. https://doi.org/10.1021/bi991343g.

23. Schwyter, D., Phillips, M., and Reisler, E. (1989). Subtilisin-cleaved actin: polymerization and interaction with myosin subfragment 1. Biochemistry *28*, 5889–5895. https://doi.org/10.1021/bi00440a027.
24. Reynolds, M.J., Hachicho, C., Carl, A.G., Gong, R., and Alushin, G.M. (2022). Bending forces and nucleotide state jointly regulate F-actin structure. Nature *611*, 380–386. https://doi.org/10.1038/s41586-022-05366-w.
25. Oosterheert, W., Blanc, F.E.C., Roy, A., Belyy, A., Sanders, M.B., Hofnagel, O., Hummer, G., Bieling, P., and Raunser, S. (2023). Molecular mechanisms of inorganic-phosphate release from the core and barbed end of actin filaments. Nat. Struct. Mol. Biol. *30*, 1774–1785. https://doi.org/10.1038/s41594-023-01101-9.
26. Orlova, A., Chen, X., Rubenstein, P.A., and Egelman, E.H. (1997). Modulation of yeast F-actin structure by a mutation in the nucleotide-binding cleft. J. Mol. Biol. *271*, 235–243. https://doi.org/10.1006/jmbi.1997.1163.
27. Orlova, A., Galkin, V.E., VanLoock, M.S., Kim, E., Shvetsov, A., Reisler, E., and Egelman, E.H. (2001). Probing the structure of F-actin: cross-links constrain atomic models and modify actin dynamics. J. Mol. Biol. *312*, 95–106. https://doi.org/10.1006/jmbi.2001.4945.
28. Belmont, L.D., Orlova, A., Drubin, D.G., and Egelman, E.H. (1999). A change in actin conformation associated with filament instability after Pi release. Proc. Natl. Acad. Sci. USA *96*, 29–34. https://doi.org/10.1073/pnas.96.1.29.
29. Boiero Sanders, M., Antkowiak, A., and Michelot, A. (2020). Diversity from similarity: cellular strategies for assigning particular identities to actin filaments and networks. Open Biol. *10*, 200157. https://doi.org/10.1098/rsob.200157.
30. Hatano, T., Alioto, S., Roscioli, E., Palani, S., Clarke, S.T., Kamnev, A., Hernandez-Fernaud, J.R., Sivashanmugam, L., Chapa-y-Lazo, B., Jones, A.M.E., et al. (2018). Rapid production of pure recombinant actin isoforms in *Pichia pastoris*. J. Cell Sci. *131*, jcs213827. https://doi.org/10.1242/jcs.213827.
31. Punjani, A., Rubinstein, J.L., Fleet, D.J., and Brubaker, M.A. (2017). cryoSPARC: algorithms for rapid unsupervised cryo-EM structure determination. Nat. Methods *14*, 290–296. https://doi.org/10.1038/nmeth.4169.
32. Johnson, P., Harris, C.I., and Perry, S.V. (1967). 3-methylhistidine in actin and other muscle proteins. Biochem. J. *103*, 79P.
33. Kumpula, E.-P., Lopez, A.J., Tajedin, L., Han, H., and Kursula, I. (2019). Atomic view into Plasmodium actin polymerization, ATP hydrolysis, and fragmentation. PLoS Biol. *17*, e3000315. https://doi.org/10.1371/journal.pbio.3000315.
34. Yao, X., Grade, S., Wriggers, W., and Rubenstein, P.A. (1999). His73, often methylated, is an important structural determinant for actin a mutagenic analysis of his73 of yeast actin. J. Biol. Chem. *274*, 37443–37449. https://doi.org/10.1074/jbc.274.52.37443.
35. Kalhor, H.R., Niewmierzycka, A., Faull, K.F., Yao, X., Grade, S., Clarke, S., and Rubenstein, P.A. (1999). A highly conserved 3-methylhistidine modification is absent in yeast actin. Arch. Biochem. Biophys. *370*, 105–111. https://doi.org/10.1006/abbi.1999.1370.
36. Wang, Y., Wu, J., Zsolnay, V., Pollard, T.D., and Voth, G.A. (2024). Mechanism of phosphate release from actin filaments. Proc. Natl. Acad. Sci. USA *121*, e2408156121. https://doi.org/10.1073/pnas.2408156121.
37. Donald, J.E., Kulp, D.W., and DeGrado, W.F. (2011). Salt bridges: geometrically specific, designable interactions. Proteins *79*, 898–915. https://doi.org/10.1002/prot.22927.
38. Yao, X., Nguyen, V., Wriggers, W., and Rubenstein, P.A. (2002). Regulation of yeast actin behavior by interaction of charged residues across the interdomain cleft. J. Biol. Chem. *277*, 22875–22882. https://doi.org/10.1074/jbc.m201685200.
39. Volkmann, N., and Hanein, D. (1999). Quantitative fitting of atomic models into observed densities derived by electron microscopy. J. Struct. Biol. *125*, 176–184. https://doi.org/10.1006/jsbi.1998.4074.
40. Stokasimov, E., McKane, M., and Rubenstein, P.A. (2008). Role of intermonomer ionic bridges in the stabilization of the actin filament. J. Biol. Chem. *283*, 34844–34854. https://doi.org/10.1074/jbc.m804419200.
41. Kudryashov, D.S., Grintsevich, E.E., Rubenstein, P.A., and Reisler, E. (2010). A nucleotide state-sensing region on actin. J. Biol. Chem. *285*, 25591–25601. https://doi.org/10.1074/jbc.m110.123869.
42. Meng, E.C., Goddard, T.D., Pettersen, E.F., Couch, G.S., Pearson, Z.J., Morris, J.H., and Ferrin, T.E. (2023). UCSF ChimeraX: Tools for structure building and analysis. Protein Sci. *32*, e4792. https://doi.org/10.1002/pro.4792.
43. Emsley, P., Lohkamp, B., Scott, W.G., and Cowtan, K. (2010). Features and development of Coot. Acta Crystallogr. D Biol. Crystallogr. *66*, 486–501. https://doi.org/10.1107/s0907444910007493.
44. Croll, T.I. (2018). ISOLDE: a physically realistic environment for model building into low-resolution electron-density maps. Acta Crystallogr. D Struct. Biol. *74*, 519–530. https://doi.org/10.1107/s2059798318002425.
45. Liebschner, D., Afonine, P.V., Baker, M.L., Bunkóczi, G., Chen, V.B., Croll, T.I., Hintze, B., Hung, L.-W., Jain, S., McCoy, A.J., et al. (2019). Macromolecular structure determination using X-rays, neutrons and electrons: recent developments in Phenix. Acta Crystallogr. D *75*, 861–877. https://doi.org/10.1107/s2059798319011471.
46. Rubinstein, J.L., and Brubaker, M.A. (2015). Alignment of cryo-EM movies of individual particles by optimization of image translations. J. Struct. Biol. *192*, 188–195. https://doi.org/10.1016/j.jsb.2015.08.007.
47. Scheres, S.H.W., and Chen, S. (2012). Prevention of overfitting in cryo-EM structure determination. Nat. Methods *9*, 853–854. https://doi.org/10.1038/nmeth.2115.
48. Chen, S., McMullan, G., Faruqi, A.R., Murshudov, G.N., Short, J.M., Scheres, S.H.W., and Henderson, R. (2013). High-resolution noise substitution to measure overfitting and validate resolution in 3D structure determination by single particle electron cryomicroscopy. Ultramicroscopy *135*, 24–35. https://doi.org/10.1016/j.ultramic.2013.06.004.

STAR★METHODS

KEY RESOURCES TABLE

REAGENT or RESOURCE	SOURCE	IDENTIFIER
Chemicals, peptides, and recombinant proteins		
chymotrypsin	Sigma	#C3142
Deposited data		
Electron potential map of yeast F-actin	This paper	EMD: EMD-51491
Atomic model of yeast F-actin	This paper	PDB: 9GO5
Experimental models: Organisms/strains		
X-33 *Pichia pastoris*	Thermofisher	C18000
Recombinant DNA		
Plasmid pPICZc-*Sc*Act1-Thy-β4-8His	Hatano et al.[30] Balasubramanian lab, University of Warwick	N/A
Software and algorithms		
CryoSparc v3.0 and 4.0	Structura Biotechnology Inc.	cryosparc.com/
ChimeraX v1.5	Meng et al.[42]	www.cgl.ucsf.edu/chimerax/
Coot v0.9	Emsley et al.[43]	https://www2.mrc-lmb.cam.ac.uk/personal/pemsley/coot/
Isolde	Croll, T.I.[44]	tristanic.github.io/isolde/
Phenix	Liebschner et al.[45]	phenix-online.org

EXPERIMENTAL MODEL AND STUDY PARTICIPANT DETAILS

Pichia pastoris, used for protein expression

Strain of *Pichia* (X-33) from ThermoScientific #C18000 carrying an integrated genetic modification ScAct1-Thyβ4-His (Hatano et al., 2018).

Pichia strains were revived from glycerol stocks by streaking out a swab of frozen cells onto YPD agar plates (1% yeast extract, 2% peptone, 2% glucose +2% agar for solid media) and incubating the inverted plates at 30°C for 2–3 days. For culture in liquid broth, a swab of cells was inoculated into YPD or MGY (1.34% YNB, 1% glycerol and 0.00004% biotin) in a conical flask and incubated at 30°C with shaking at a speed of 220 rpm. All *Pichia* growth conditions were based on the EasySelect *Pichia* Expression Kit Instruction Manual (Invitrogen).

For storage, cells were streaked for single colonies on YPD agar. A single colony was then grown to form a lawn of cells over an entire agar plate surface. All growth from one plate was scraped into a cryovial and resuspended in YPD +15% glycerol to make a concentrated cell suspension. Glycerol stocks were flash-frozen in liquid N_2 and stored at −80°C.

METHOD DETAILS

Yeast actin purification

The *Pichia pastoris* yeast strain used in this study to express *S. cerevisiae ACT1* was a kind gift from the Balasubramanian lab (University of Warwick). This strain is the X-33 *Pichia pastoris* strain (ThermoScientific) carrying an integrated plasmid (pPICZc-*Sc*Act1-Thy-β4-8His). This allowed expression of a thymosin beta-4-actin fusion. When this fusion protein is expressed, the Thyβ4 sequesters the recombinant G-actin, preventing interactions with both the barbed and pointed end of the monomer (Figure 1C). Crucially, the bound thyβ4 makes the recombinant actin unavailable for polymerization with the native pool of *Pichia* G-actin. Expression is under control of the AOX1 promoter allowing expression to be induced on addition of methanol to the growth medium. Cells were grown and induced to express *S. cerevisiae* actin as described.[30] The actin was purified according to the published protocol with chymotrypsin cleavage being used to release the purified actin from the fusion as a chymotrypsin site is available immediately after the final actin residue Phe375.[30]

Cells were broken at the University of Warwick. 30 g of frozen cells were loaded into grinder tubes (#6751, SPEX SamplePrep) pre-cooled with liquid N_2 and ground in a freezer mill (#6870, SPEX SamplePrep) in a liquid N_2 bath for 1 min with 14 cycles/s. Grinding was repeated 30 times at 1 min intervals.

Lysate powder was dissolved in an equal amount of 2x binding buffer [20 mM imidazole, 20 mM HEPES pH 7.4, 600 mM NaCl, 4 mM MgCl2, 2 mM ATP, 2× concentration of protease inhibitor cocktail (Complete, EDTA free #05056489001, Roche), 1 mM phenylmethylsulfonyl fluoride (PMSF) and 7 mM β-mercaptoethanol (β-ME)]. Lysate was sonicated on ice (10 s with 60% amplitude, Qsonica Sonicators) until all aggregates were resolved. Lysate was centrifuged at 4°C at 3220g for 15 min (Eppendorf #A-4-81 rotor) then further cleared by centrifugation at 4°C at 25658g for 1 h (Thermo Fisher Scientific, #A23-6×100 rotor). Supernatant was passed through a 0.22 μm filter (Corning #431097) and incubated with 1 mL nickel resin (Thermo Scientific, #88222) at 4°C for 1–1.5 h.

Resin was pelleted down by centrifugation at 4°C at 1258g for 5 min (Eppendorf #A-4-81 rotor) and washed with 25 mL ice-cold binding buffer [10 mM imidazole, 10 mM HEPES pH 7.4, 300 mM NaCl, 2 mM MgCl2, 1 mM ATP, protease inhibitor cocktail (cOmplete, EDTA free #05056489001, Roche), 1 mM PMSF and 7 mM β-ME]. Resin was loaded into an open column (Bio-Rad, #731–1550) and washed with 20 mL ice-cold binding buffer, followed by 45 mL ice-cold G-buffer [5 mM HEPES (pH 7.4), 0.2 mM CaCl2, 0.01% (w/v) NaN3, 0.2 mM ATP and 0.5 mM dithiothreitol (DTT)]. Resin was resuspended in 6 mL ice-cold G-buffer containing 5 μg/mL TLCK-treated chymotrypsin (Sigma, #C3142-10MG) and incubated overnight at 4°C. Chymotrypsin was inactivated by addition of PMSF to 1 mM and incubated for 30 min on ice.

Eluate was collected and actin retained on the resin was eluted with 12 mL G-buffer and all the elution fractions combined. Eluate was then concentrated using a 30 kDa cut-off membrane (Sigma-Aldrich, #Z677892-24EA) and the final volume adjusted to 900 μL with ice-cold G-buffer. Actin was polymerized by addition of 100 μL 10× MEK buffer [20 mM MgCl2, 50 mM glycol-bis(2-aminoethylether)-N,N,N′,N′-tetraacetic (EGTA) and 1 M KCl], for 1 h at room temperature. F-actin was pelleted by ultracentrifugation for 1 h at room temperature at 45,000 rpm (Beckman TLA-55 rotor) and re-suspended in 1 mL ice-cold G-buffer. F-actin was depolymerized by dialysis against 1 L G-buffer at 4°C for 2 days. Dialysis buffer was exchanged every 12 h. Any remaining F-actin was pelleted by ultracentrifugation at room temperature at 45,000 rpm for 30 min (Beckman TLA-55 rotor) and actin in the supernatant was concentrated to 100 μM using a 30 kDa cut-off membrane (Sigma-Aldrich, #Z677892-24EA). The concentration of actin was determined by measuring the absorbance at 290 nm using a NanoDrop 2000c spectrophotometer (Thermo Fisher Scientific).

For the experiments here the concentration of the preparation was 25 μM (approx. 10.5 mg/mL). Actin was kept in G-buffer: 10 mM Tris (pH 7.5), 0.2 mM CaCl2, 0.2 mM ATP (pH 7.0), 0.5 mM DTT. Polymerization competence was verified in a sedimentation assay following addition of polymerization salts (KME) to a 50 μL assay volume containing 3 μM actin (KME - 50 mM KCl, 1 mM MgCl2, 1 mM EGTA, 10 mM Tris (pH 8.0). Samples were left for 1 h at room temperature (20°C) prior to centrifugation at 90,000 rpm in a Beckman ultracentrifuge for 15 min.

Polymerization of actin for CryoEM

Freshly prepared G-buffer was used to dilute G-actin giving a final sample volume of 20–30 μL. 10x KME polymerization salts were added to 1x final. Polymerization was allowed to occur at room temperature for approximately 1 h.

CryoEM grids were prepared using a Leica EM GP automatic plunge freezer (Leica Microsystems). An optimal concentration of 1 μM G-actin was used. At this concentration the filament density on the grid was high with limited filament overlap. 3 μL of actin was added to copper Quantifoil R2/2 300 mesh holey carbon grids. Excess liquid was blotted for 5 s from the mesh side of the grid (back blotting) and the grids were plunge-frozen in liquid ethane. Frozen grids were stored in liquid nitrogen until imaged.

CryoEM data collection and image processing

CryoEM images were collected on a Titan Krios microscope (ThermoFisher Scientific) operated at 300 kV and recorded on a K3 direct electron detector (Gatan Inc.) operated in super-resolution mode. The images were collected at a nominal magnification of 105,000× such that the object level pixel size was 0.834 Å/pixel (super-resolution pixel size of 0.417 Å/pixel). The images were recorded as 2.3 s movies divided into 27 frames. The total dose was 27 electron/Å^2 and the fluence was 1 electron/Å^2/frame.

All image processing jobs and three-dimensional (3D) reconstructions were performed using CryoSPARC (versions 3 and 4)[31] (Structura Biotechnology Inc.). The individual super-resolution movie frames were binned by 2 and the frames were aligned using alignparts_lmbfgs[46] as implemented within Cryosparc. The contrast transfer function (CTF) of the aligned micrographs was estimated using the patch CTF routine of Cryosparc. After removing unsuitable micrographs (0.5 CTF fit resolution worse than 6 Å and average intensity higher than 3.8), 2540 micrographs were retained for further processing.

Particles were identified using template free filament tracer and extracted with a box size of 880 Å (the large box size allowed inclusion of two helical turns) and downscaled to a pixel size of 2 Å/pixel. At this stage 559,574 particles were selected. These particles were subjected to one round of 2D classification and 267,843 particles contributing to selected optimal 2D class averages (determined by visual inspection) were retained for further processing.

These particles were used to perform an initial helical reconstruction resulting in a 4 Å map. Using the particle orientation determined from the initial refinement as a starting point, the symmetry parameters were further refined. 2D templates were generated from this initial 3D map and used for a second round of template-based particle picking resulting in 2,058,503 particles. These particles were refined using the initial helical parameters as a starting point. resulting in a 2.8 Å map. This was followed by refinement of the defocus values of each particle and the beam tilt and higher order aberrations were estimated for each micrograph. Another round of helical refinement was performed using the updated CTF parameters. For this round the non-uniform refinement routine was used along with a finer search of the helical symmetry parameters providing the parameters listed in Table S1. This led to a map with a nominal resolution of 2.5 Å. In order to ensure that the reconstruction was not trapped in a local symmetry minimum, the refinement

was repeated without applying helical symmetry and the resulting structure was identical to the one obtained with helical symmetry (data not shown).

The resolutions of the CryoEM maps were estimated from the gold standard Fourier Shell Correlation (FSC) curves[47] calculated in CryoSPARC and are reported according to the 0.143 cutoff criterion. The FSC curves were corrected for the convolution effect of a soft mask applied to the half-maps using phase randomization.[48] To prevent overfitting during refinement, it was ensured that particles picked from the same filament were placed in the same half-set for gold standard FSC resolution estimation. The local resolution of the map was calculated in Cryosparc using the 0.143 FSC criterion.

Model building and refinement

Coordinates for one subunit of rabbit F-actin (PDB ID:8A2T)[5] were fitted into the sharpened CryoEM using the 'Fit in Map' tool in ChimeraX.[42] The fitted model was examined in Coot,[43] residues mutated to those of yeast where required and missing residues in the D loop built in. Fits of side chain rotamers and main chain were optimized either by real space refinement within Coot or in ChimeraX/Isolde.[44]

Five copies of the subunit were fitted into the helical density of the CryoEM map and subjected to real space refinement within Phenix,[45] with non-crystallographic symmetry (NCS) constraints applied and refined. A central subunit of the refined structure was rebuilt where necessary to optimize geometry and clashes. A new filament model was built from this subunit using the refined symmetry operators and subjected to further cycles of real space refinement and rebuilding.

Putative water molecules were added automatically in Coot with a 3 sigma density threshold around one central subunit. These were inspected manually and any found in noisy or highly asymmetric density were removed. NCS was applied to generate a five-subunit model and any clashing waters or waters with no clear hydrogen bonding interactions were removed. A final cycle of NCS constrained refinement in Phenix was performed with a final five-subunit filament model generated from the central refined protomer.

QUANTIFICATION AND STATISTICAL ANALYSIS

The CryoEM datasets were processed using CryoSPARC v3.0 and 4.0, then analyzed using ChimeraX v1.5, Coot v0.9, Isolde and Phenix. The statistical information generated from data processing, refinement, and validation is shown in Table S1. Cryo-EM data collection and refinement statistics are summarized in Table S1.